JPEDAV (2016) 37:491–502
DOI: 10.1007/s11669-016-0481-z
1547-7037 ©ASM International

Precipitation Modeling of Multi-Component Nickel-Based Alloys

W. Cao, F. Zhang, S.-L. Chen, C. Zhang, J. Zhu, S. L. Semiatin, and J. S. Tiley

(Submitted February 29, 2016; in revised form April 20, 2016; published online June 24, 2016)

Computer aided materials design is of increasingly importance and interest because the conventional approach solely relying on experimentation is no longer viable within the constraint of available resources. The CALPHAD approach, which emerged first as an approach for the calculation of phase equilibria and thermodynamic properties of complex multi-component, multi-phase systems, has in recent years been applied to a broader field of materials science and engineering beyond phase diagrams, such as solidification, coating, joining, and phase transformation. This approach, therefore, plays an important role in modern materials design in the framework of Integrated Computational Materials Engineering. In this study, we present a modeling approach that integrates thermodynamic calculation and kinetic simulation to simulate the precipitation kinetics of multi-component alloys. Its applications will be demonstrated by the studies of a number of nickel-based alloys.

Keywords alloy design, integrated computational materials engineering, materials informatics, nickel-based alloys, precipitation modeling

1. Introduction

It is a common practice for materials scientists/engineers to design new materials or improve the existing ones with desired properties through the optimization of alloy chemistry and processing conditions. Traditionally, this process has been relying on pure experimentation and following a trial-and-error approach, which is costly and time-consuming. However, with the recent advancement of computational materials engineering and modern information technology, the alloy design process can be greatly accelerated with the aid of modeling tools at multiple length-scales such as the first-principles calculation at nano-meter scales, phase field modeling from nano-meter scales to mill-meter scales, and the computational thermodynamics/kinetics for bulk materials based on the CALPHAD method.[1] These modeling tools, when integrated under the framework of Materials Informatics or Integrated Computational Materials Engineering (ICME)[2–4] and combined with key experiments, make the materials design process much more focused and cost-efficient.

By following such an approach, the present study focuses on developing an integrated modeling framework that can be used to understand thermodynamics and precipitation kinetics of multi-component alloys during phase transformation. Precipitation hardening, or age hardening, provides one of the most widely used mechanisms for the strengthening of many structural materials including aluminum alloys, nickel-based superalloys, titanium alloys, magnesium alloys and some stainless steel alloys. It relies on the significant decrease in solid solubility with decreasing temperature to produce the dispersed second-phase particles, which impede the movements of dislocations or defects in the crystal lattice, thereby hardening the material.

Modeling of precipitation process plays an important role in understanding the behavior of materials and thus has increasingly gained interests from both scientific and practical points of view. As a matter of fact, many efforts have been devoted to the modeling of the microstructure and the correlated hardening responses during the precipitation process for different types of materials.[5–14] However, precipitation is a complex process involving the simultaneous occurrence of nucleation, growth and coarsening. Accurate modeling of the precipitation process requires a synchronous consideration of all these contributions to simulate the temporal evolution of microstructure and the corresponding responses of mechanical properties. Moreover, the phase equilibrium information as well as the composition and mobility data of matrix phase need to be constantly updated as the nucleation, growth and coarsening proceed. Such a simulation, therefore, necessitates a smooth integration of thermodynamic calculation, kinetic simulation and property modeling of the material. Nevertheless, most of previous modeling efforts have been focusing on only one or two aspects of the problem[6–21] and an integrated framework coupling reliable thermodynamic calculation, kinetic simulation and property prediction of multi-component systems for industrial applications is rarely available.

In these regards, we have developed PanPrecipitation[22,23] module as a new module of PANDAT software.[22,24] It is fully

W. Cao, F. Zhang, S.-L. Chen, C. Zhang, and **J. Zhu**, 8401 Greenway Blvd., Suite 248, Middleton, WI 53562, USA; **S. L. Semiatin** and **J. S. Tiley**, Air Force Research Laboratory, Materials and Manufacturing Directory, AFRL/RXCM, Wright-Patterson Air Force Base, Dayton, OH 45433, USA. Contact e-mail: Fan.Zhang@computherm.com.

coupled with the thermodynamic calculation engine—PanEngine which provides reliable thermodynamic properties and mobility data necessary for the precipitation simulation. PanPrecipitation has three built-in kinetic models for microstructure simulation at multi-levels: (1) the well-known JMAK model (Johnson-Mehl-Avrami-Kolmogorov)[15–18,25] for estimation of the overall transformation rate, (2) the Fast-Acting model based on Langer and Schwartz theory[14] for simulation of the evolution of particle number density and mean size, (3) and the more advanced Kampmann and Wagner Numerical (KWN) model[9] for the predication of the full evolution of the particle size distribution (PSD) in addition to average quantities. The obtained microstructure information (e.g., volume fraction, number density, mean size and particle size distribution) can subsequently be used to predict the age hardening behavior on the basis of the proposed strengthening models.[6,8,11,26]

In this paper, we will first give a brief review of the CALPHAD method in section 2; we will then present the nucleation and growth models in section 3; the applications will then be demonstrated by a number of multi-component nickel-based alloys in section 4. Finally, the major advantages and some limitations of the current approach will also be discussed in section 5.

2. CALPHAD Approach

2.1 Thermodynamic Modeling

The CALPHAD approach,[1] being able to describe the thermodynamic properties of multi-component, multi-phase systems, has become critically important in materials design and process optimization. The essence of this approach is to obtain self-consistent thermodynamic descriptions of the lower-order systems, binaries and ternaries, in terms of available thermodynamic and phase equilibrium data. Based on the known descriptions of the constituent lower-order systems, thermodynamic descriptions (normally called "thermodynamic database" or just "database") for higher-order systems can be obtained via an extrapolation method.[27] In the CALPHAD approach, the Gibbs energy of each phase is described by a thermodynamic model and the three most-commonly used models are the line compound model for stoichiometric phases, the substitutional solution model for disordered solution or liquid phases and the compound energy formalism (CEF) for ordered intermetallic phases.[28,29] Advanced thermodynamic models were also developed such as the associate and the ionic two-sublattice models for the liquid phases.[30] More recently the cluster/site approximation (CSA),[31–33] a simplified CVM,[34] was developed to describe the order/disorder phase transformation for solid alloys. It can also be used to model liquid alloys exhibiting short-range ordering. We will not discuss these models here and readers are referred to the references for details. The significant achievement of the CALPHAD approach is that separately measured thermodynamic data and phase equilibrium data can be used to develop a set of self-consistent Gibbs energy functions, i.e., a thermodynamic database for a system of interest. Such a thermodynamic database enables one to readily calculate phase equilibria and thermodynamic properties not experimentally available of multi-component systems. Furthermore, other properties, such as chemical driving force and thermodynamic factors, can also be calculated using such a thermodynamic database. These properties can be integrated with mobility data (to be discussed in section 2.2) for the simulation of diffusion processes and diffusion controlled precipitation kinetics.

2.2 Mobility Modeling

Mobility data is essential in the simulation of microstructural evolution. Variety types of experimentally measured diffusion data can be found in the literature, such as self-diffusivities, inter-diffusivities, and so on. A convenient and widely-used approach is to choose atomic mobilities as the stored data and establish a mobility database.[35] It is straightforward to calculate the diffusion coefficients on the basis of these data and known thermodynamics. For example, the diffusion coefficient defined in the volume-fixed frame of reference, D^V_{kj}, can be calculated by a product of a mobility term and a thermodynamic factor,

$$D^V_{kj} = \sum_{i=1}^{n} (\delta_{ik} - x_k) \cdot x_i \cdot M_i \cdot \frac{\partial \mu_i}{\partial x_j} \qquad \text{(Eq 1)}$$

where j is the diffusing specie, k the gradient specie, δ_{ik} the Kroncker delta, M_i the mobility of the specie i in a given phase, x_i the mole fraction of component i, and $\frac{\partial \mu_i}{\partial x_j}$ the thermodynamic factor, which can be easily retrieved from the aforementioned thermodynamic database. These relationships also correlate the parameters stored in a mobility database with the experimental data. The mobility database is thus developed by optimizing the parameters in terms of experimentally measured value. Since diffusion is a thermally activated process, the atomic mobility of a component in a specific structure is described as an Arrenius-type expression,

$$M_i = \Omega_i \frac{1}{RT} \exp\left(-\frac{\Delta Q^*_i}{RT}\right) \qquad \text{(Eq 2)}$$

where Ω_i is the product of the atomic jump distance and the jump frequency, and ΔQ^*_i is the diffusion activation energy of a specie i in a given phase. These two parameters can be combined into one by taking Ω_i to be 1. The activation energy, ΔQ^*_i, frequently taken to be temperature and composition dependent, is expressed in terms of a Redlich-Kister[36] polynomial,

$$\Delta Q^*_i = \sum_j x_j \cdot Q^j_i + \sum_p \sum_{j>p} x_p \cdot x_j \cdot \sum_k A^{pj}_k \cdot (x_p - x_j)^k \qquad \text{(Eq 3)}$$

where Q^j_i and A^{pj}_k are linear functions of temperature. The composition dependence following this polynomial is similar to the one used to describe excess Gibbs energy of solution phase. Optimization of the parameters in the activation energy follows the same strategy as that in the

development of thermodynamic database, and the model parameters for the activation energy need to be developed for binaries and key ternaries. In this work, the mobility database for nickel alloys provide key inputs for the simulation of diffusion-controlled precipitation process, which will be presented in section 4.

3. Microstructure Modeling

3.1 Nucleation, Growth and Coarsening

It has been noted earlier that the precipitation process typically involves the simultaneous occurrence of nucleation, growth and coarsening. This point can be illustrated by considering the precipitation kinetics of the two well-studied model alloys: Cu-1.02 at.% Co and Ni-14 at.% Al. Figure 1(a) and (b) show the Cu-rich end of the Cu-Co and Ni-rich end of the Ni-Al phase diagrams respectively. For the case of Cu-1.02 at.% Co, it forms *fcc* (Cu) solid solution when the alloy is held at a temperature above the solvus but below the solidus, e.g., 950 °C. After quenching the alloy to a lower temperature, e.g., 600 °C, the solid solution *fcc* (Cu) phase will become supersaturated with respect to Co and

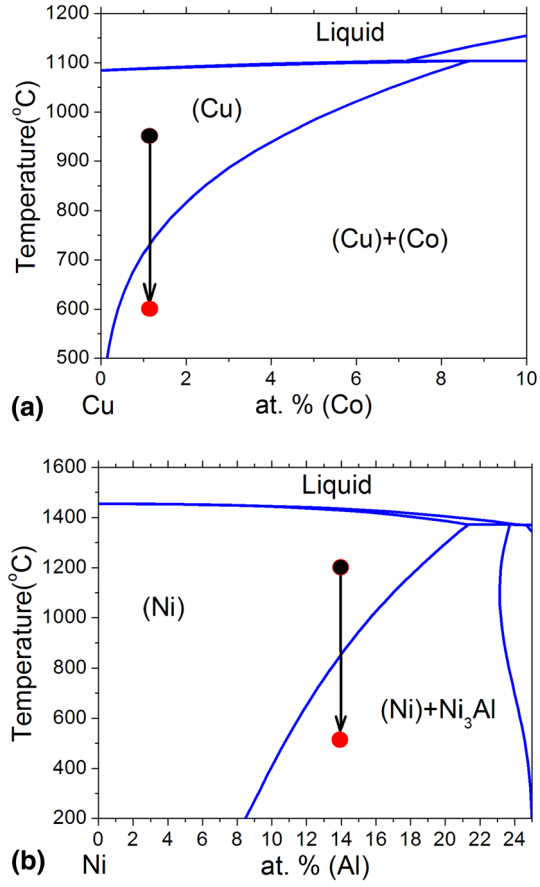

Fig. 1 (a) Cu rich end of the Cu-Co phase diagram with the Cu-1.02 at.% Co alloy; (b) Ni rich end of the Ni-Al phase diagram with the Ni-14 at.% Al alloy

there is a driving force for the precipitation of the *fcc* (Co) phase. For the other case of Ni-14 at.% Al, the disordered *fcc* (Ni) solid solution, which is usually referred as the γ phase, is stable in the temperature range from the solidus to the solvus. Below the solvus temperature, γ′-Ni_3Al precipitates from the solid solution. The γ′ phase has the ordered *L*12 structure. In fact, the precipitation processes of these two alloys as indicated in Fig. 2 and 3 are quite different.

Figure 2 shows the evolution of the precipitation process of the alloy Cu-1.02 at.% Co aged at 600 °C. Following an incubation time, nucleation and growth of the (Co) phase begin, leading to increases in particle number density, average size, and volume fraction, and concomitantly decreases in the chemical driving force and solute concentrations in the matrix phase. It is worth pointing out that a plateau period is observed in this case, which happens after the nucleation is effectively complete and the coarsening has yet to begin. Only after such a period is over at about 2 h ageing, the Gibbs-Thomson effect and Ostwald coarsening become significant and predominant. In other words, the coarsening and nucleation processes do not overlap in this case.[19] By contrast, as shown in Fig. 3, the precipitation of the alloy Ni-14 at.% Al (aged at 550 °C) indicates a significant overlap of nucleation, growth and coarsening processes due to the small value of (γ/γ′) interphase boundary energy and the resulted large number of particles that interfere with each other and thus lead to the coarsening of larger particles at the expense of smaller ones in the very early stage of precipitation.

As can be seen, nucleation, growth, and coarsening constitute three basic processes for the precipitation phase transformation. Traditionally, these three processes have often been considered separate from each other with the implicit assumption that one stage goes to completion before the next stage begins. However, from the above two examples and recent studies by Kampmann and Wagner,[9] and Robson,[12,19] it reveals that the nucleation, growth, and coarsening may occur concurrently, and therefore the

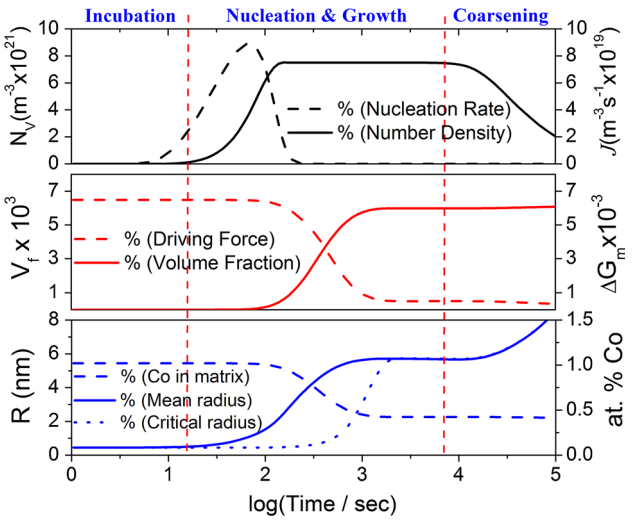

Fig. 2 Precipitation evolution of the Cu-1.02 at.% Co alloy ageing at 600 °C

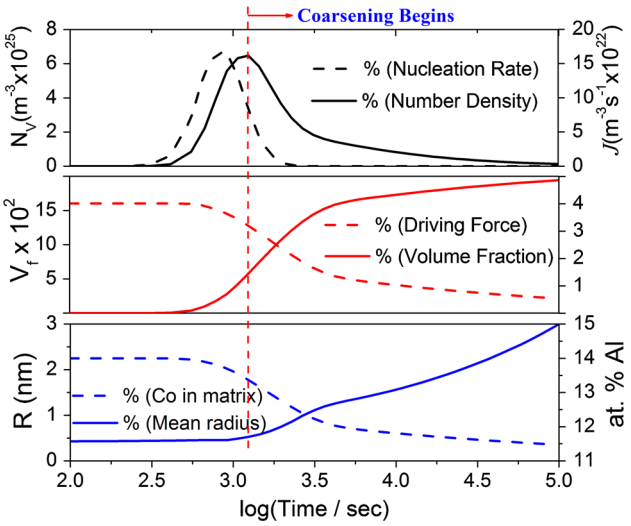

Fig. 3 Precipitation evolution of the Ni-14 at.% Al alloy ageing at 550 °C

precipitation kinetics depends on the rates of all three processes.

To address this situation, the present study adopted two theoretical models that were modified to account for the simultaneous nucleation, growth and coarsening in multi-component and multi-phase alloys. The first one is the so-called Fast-Acting model, which is developed based on the Langer and Schwartz theory[14] and can predict the evolution of particle number density and average size. The other one is the KWN model, which is based on the Kampmann and Wagner's numerical framework[9] and predicts the full evolution of particle size distribution in addition to the average quantities. These kinetic models at different levels provide a wide range of selections for a variety of industrial applications.

3.2 The Kinetic Models

In the present study, the KWN model is based on the Kampmann and Wagner's work as implemented in a numerical framework,[9] and extended to handle both homogeneous and heterogeneous nucleation, dealing with various morphologies for the simulation of co-precipitation kinetics of multi-component alloys under arbitrary heat treatment conditions. The following gives a brief introduction to the KWN model along with its sub-models for nucleation, growth and coarsening. More detailed descriptions can be found in literatures.[9,13,19,22]

Specifically, in the KWN model the continuous particle size distribution is divided into a large number of size classes. The program takes a simulation step at every sample time hit. To maintain both accuracy and efficiency between two adjacent simulation steps, a fifth-order Runge-Kutta scheme is used to generate an adaptive step size based on the continuity equation.

At each simulation step, the number of new particles is first calculated using classical nucleation theory and then these new particles are allocated to an appropriate size class. The transient nucleation rate is given by,

$$J = N_v Z\beta^* \exp\left(-\frac{\Delta G^*}{R_g T}\right)\exp\left(\frac{-\tau}{t}\right) \quad \text{(Eq 4)}$$

The pre-exponential terms in Equation 4 are:N_v, the nucleation site density, Z, the Zeldovich factor and β^*, the atomic attachment rate. t is the time, τ the incubation time for nucleation, R_g the gas constant and $T$the temperature. The nucleation barrier is defined as $\Delta G^* = \frac{4\pi}{3}(R^*)^2\sigma$ whereR^* is the radius of the critical nucleus and $R^* = \frac{-2\sigma V_m}{\Delta G_m}$. The nucleation barrier can then be written as,

$$\Delta G^* = \frac{f\sigma^3}{\Delta G_m^2 / V_m^2} \quad \text{(Eq 5)}$$

with $f = \frac{16\pi}{3}$ for homogeneous nucleation of spherical nuclei. V_m is the molar volume of the precipitate phase and ΔG_m is the molar chemical driving force for nucleation. σ is the interfacial energy of the matrix/particle interface. The multi-component version of the parameters has been proposed by Kozeschnik et al.[37] and implemented in the current study. In order to account for the heterogeneous nucleation, the nucleation site density N_v in Equation 4 and f in Equation 5 are treated as phenomenological parameters that can be adjusted in terms of available experimental data

Next, the growth of existing particles for each size class is computed by assuming diffusion-controlled growth, where the Gibbs-Thomson size effect is also taken into account. The growth model for multi-component alloys is modified by Wu[23] based on that proposed by Morral and Purdy[38] so that it handles the growth/dissolution of various precipitate phases with different morphologies. The motion rate of the curved interface, e.g., the interface of a spherical or lens-like precipitate, and the edge of a plate-like precipitate, is given by,[23]

$$v = \frac{dR}{dt} = \frac{K}{R}\left(\frac{2\sigma V_m}{R^*} - \frac{2\sigma V_m}{R}\right) \quad \text{(Eq 6)}$$

where R is the radius of the interface. R^* is the radius of the critical nucleus, and

$$K = \frac{1}{(\Delta C^{\alpha\beta}][M]^{-1}[\Delta C^{\alpha\beta})} \quad \text{(Eq 7)}$$

$\left(\Delta C^{\alpha\beta}\right]$ and $\left[\Delta C^{\alpha\beta}\right)$ are the row and column vector of the solute concentration difference between α (matrix phase) and β (precipitate phase), and $[M]$ is the chemical mobility matrix. One can verify that Equation 6 can be further simplified and written as,

$$v = \frac{dR}{dt} = \frac{K}{R}\Delta G_m^* \quad \text{(Eq 8)}$$

where $\Delta G_m^*$is the transformation driving force defined as $\Delta G_m^* = \Delta G_m - \Delta G_T$ with ΔG_m being the molar chemical driving force and $\Delta G_T = \frac{2\sigma V_m}{R}$ compensating the energy difference due to the Gibbs-Thompson effect.

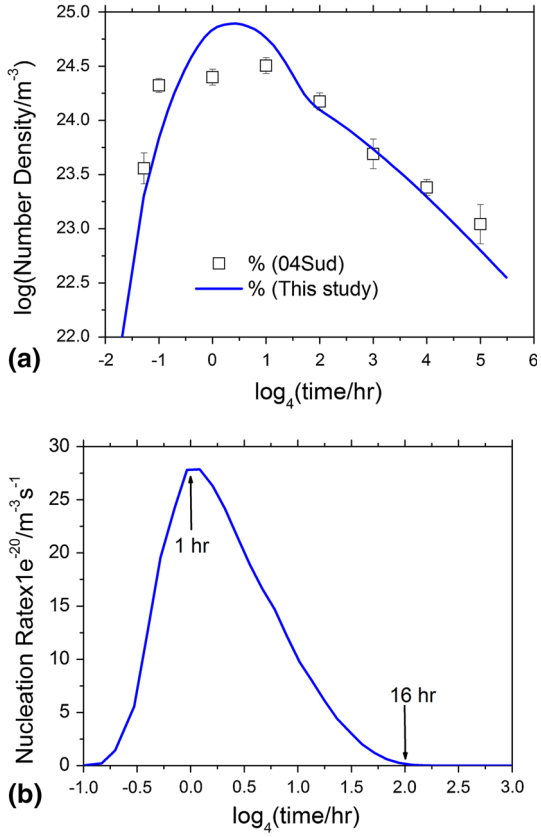

Fig. 4 The predicated temporal evolution of γ' (a) number density compared with the experimental data by 04Sud[42]; (b) nucleation rate in the alloy Ni-5.2Al-14.2Cr at.% aged at 600 °C

Finally, the particle size distribution and the volume fraction of the particles are updated and the matrix composition is re-calculated according to the mass conservation Equation 9 in the end of each simulation step. The updated values are then used in the next time step.

$$C_i^* = \left(1 - \sum_P^{n_P} \phi_P\right) C_i^\alpha + \sum_P^{n_P} \phi_P C_i^P \qquad \text{(Eq 9)}$$

where C_i^* is the initial concentration of component i, ϕ_P is the mole fraction of precipitate phase P, n_P is the number of precipitate phases, C_i^α is the concentration of component i in the matrix α phase, and C_i^P is the concentration of component i in precipitate phase P.

It should be noted that coarsening in the KWN model arises naturally and becomes dominant when the supersaturation is sufficiently low. In the Fast-Acting model, however, the coarsening is considered explicitly. Accordingly, a model based on the LSW theory [10,39] is employed, which characterizes the curvature-driven particle growth. The multi-component version can be written as,

$$\bar{R}^3 - \bar{R}_0^3 = \frac{4}{9} K(t - t_0) \qquad \text{(Eq 10)}$$

where $\bar{R}$ is the average particle radius at time t, $\bar{R}_0$ is the average particle radius at t_0, the time at the onset of

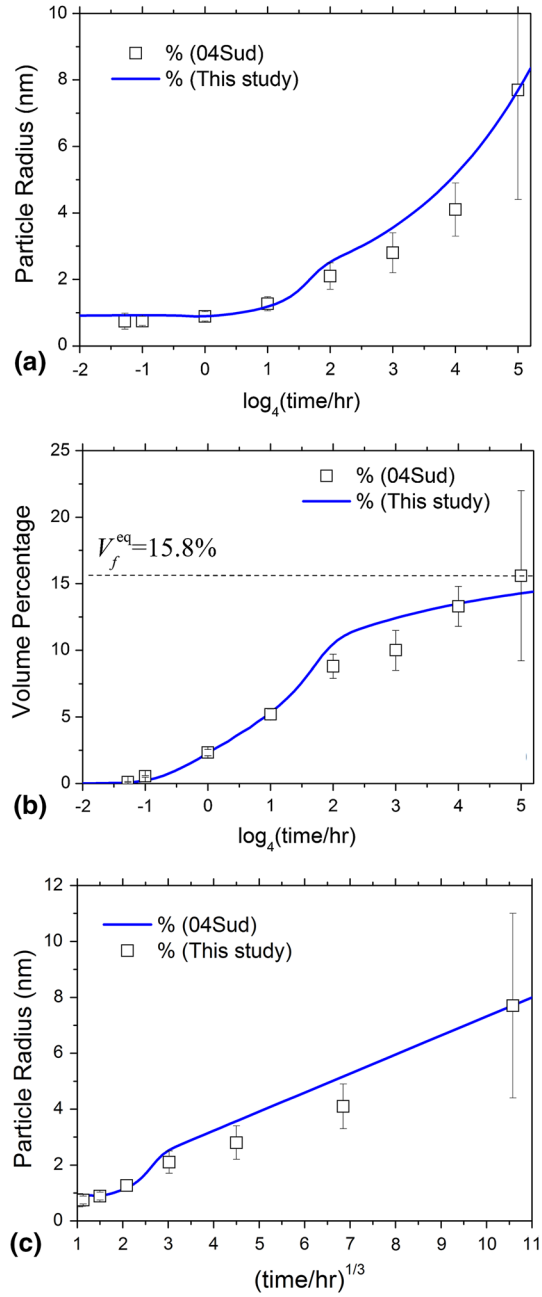

Fig. 5 The predicated temporal evolution of γ′ (a) mean size in log scale; (b) volume fraction; (c) mean size vs. $t^{1/3}$ in the alloy Ni-5.2Al-14.2Cr at.% aged at 600 °C compared with the experimental data by 04Sud[42]

coarsening. It should be noted that for Ni-based superalloys, the nucleation/growth takes place quickly and the coarsening process usually begins in the very early stage. In this case, a value of $t_0 = 0$ is assumed and this assumption is consistent with the simulation and experimental observation to be discussed in section 4.2. K is a physical property that appears also in LSW theory for the coarsening of binary alloys. Morral and Purdy[38] derived an equation for K that applies to multicomponent alloys, which was first applied to

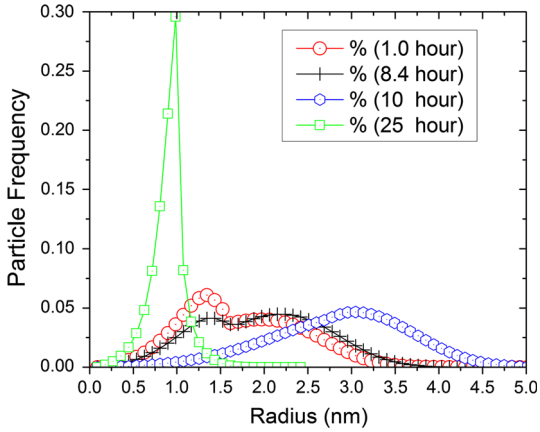

Fig. 6 The predicated γ' particle size distributions at different times: 1.0, 8.4, 10, and 25 h in the alloy Ni-5.2Al-14.2Cr at.% aged at 600 °C

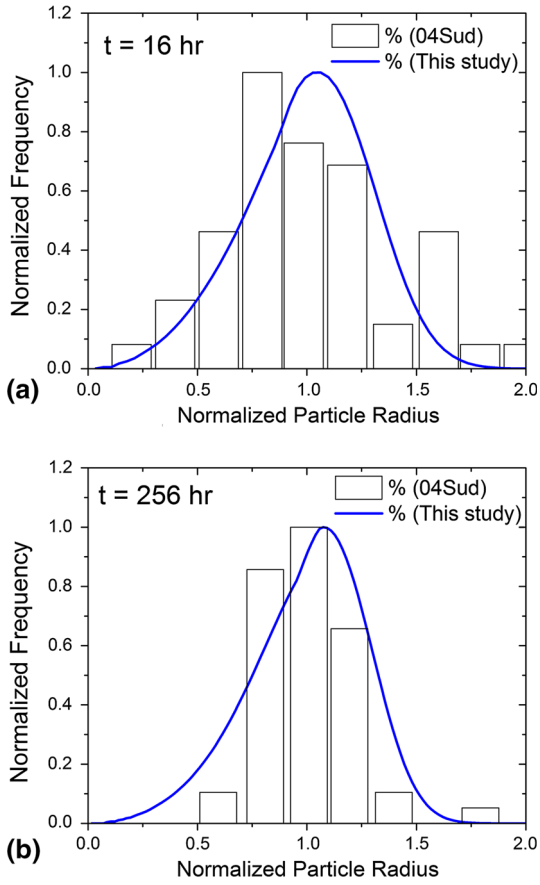

Fig. 7 The predicated γ' particle size distributions at (a) 16 h and (b) 256 h in the alloy Ni-5.2Al-14.2Cr at.% aged at 600 °C compared with the experimental data by 04Sud[42]

KWN theory as well by Wu[23] and this work as well. In the meantime, the model accuracy and efficiency are also ensured by controlling the adaptive step size with a fifth-

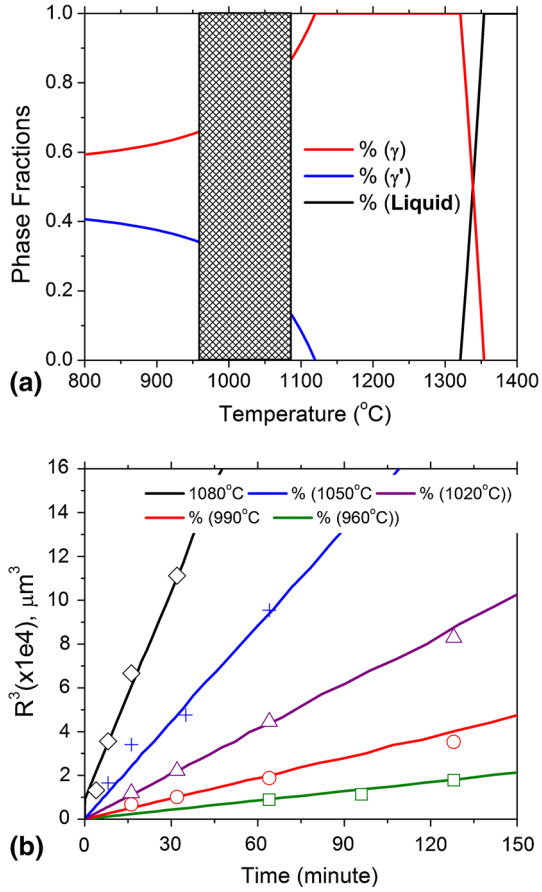

Fig. 8 (a) Phase fractions of liquid, γ and γ' as a function of temperature for Alloy Rene88DT showing the temperature window where the experimental data are available; (b) The predicated temporal evolution of mean γ' size in Alloy Rene88DT aged at different temperatures 960, 990, 1020, 1050 and 1080 °C compared with the experimental data[44]

order Runge-Kutta scheme. At each simulation step, the same nucleation and growth models, as given in Equation 4 and 8, are used for the estimation of the average size changes.It is worth mentioning that the thermodynamic equilibrium information (e.g.,$\left(\Delta C^{\alpha\beta}\right]$ and $\left[\Delta C^{\alpha\beta}\right)$ in Eq 7; C_i^{α} and C_i^{P} in Eq 9), the driving force (e.g., ΔG_m in Eq 4 and 8) and the mobility data (such as $[M]$ in defining the kinetic parameter) needed for KWN simulations are obtained directly from thermodynamic calculation engine. Therefore, no assumptions and initial values are required for each simulation step.

4. Results and Discussions

The Nickel-based superalloys have been widely used as high-temperature structural materials in gas turbine engine applications for many years. The excellent mechanical properties of these materials at elevated temperatures are

Table 1 Alloy chemistry of LSHR provided by AFRL

Comp	Al	B	C	Co	Cr	Mo	Nb	Ti	Ta	Zr	W	Ni
wt.%	3.6	0.02	0.03	20.5	12.4	2.8	1.5	3.5	1.2	0.05	4.3	bal

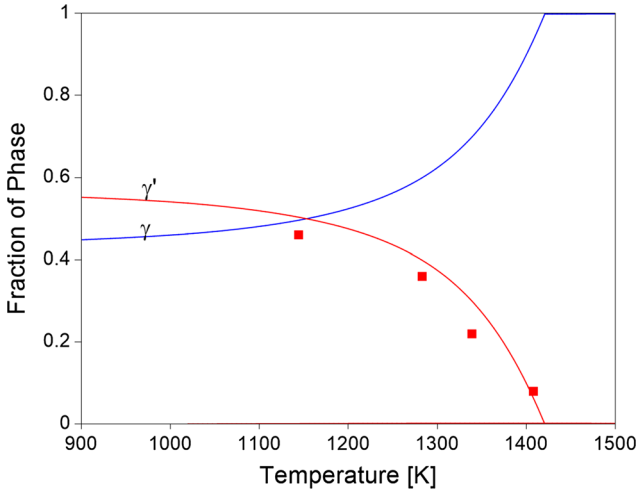

Fig. 9 Calculated fraction of γ and γ′ as a function of temperature

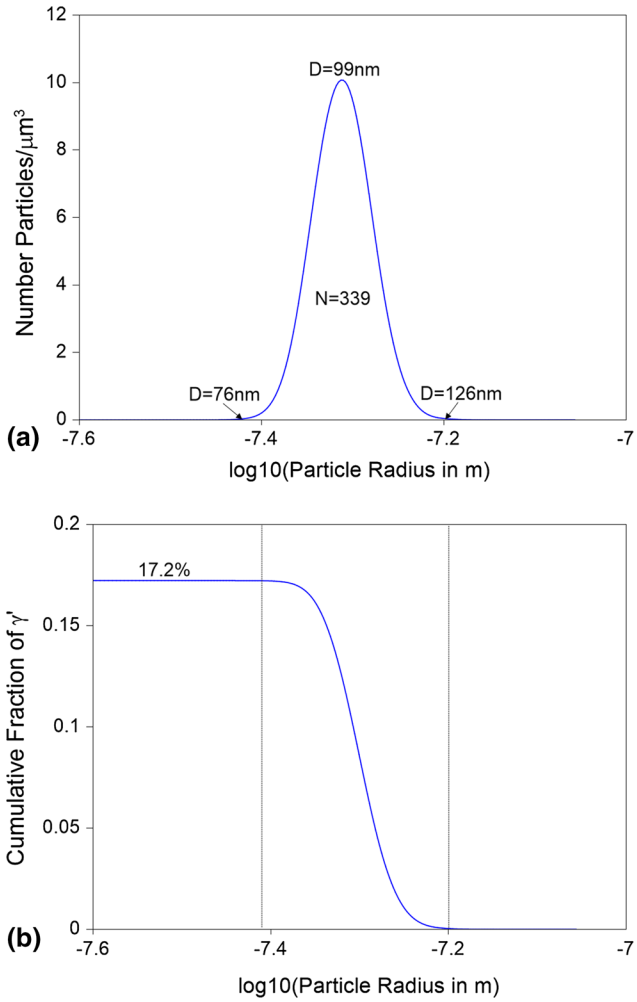

Fig. 10 Distribution and the cumulative fraction of γ′ precipitates as a function of particle size cooled to 1389 K at the speed of 139 K/min

generally attributed to the precipitation of nanometer-sized second-phase particles (γ′, the ordered $L1_2$ phase) from the solid-solution matrix (γ, the disordered *fcc* structure). For most Nickel-based alloys, the two phases can accommodate negligible lattice parameter misfits and exhibit nearly perfect coherent interphase boundary with very small interfacial energy. It is therefore of scientific and practical interests in modeling different stages of the precipitation process for those technologically important Ni-based superalloys. In the current work, PanPrecipitation was used to study: (1) the early stages of precipitation in a ternary alloy Ni-5.2Al-14.2Cr at.% with the KWN model; (2) the coarsening behavior of a commercial Rene88DT alloy with the Fast-Acting model; (3) the precipitation kinetics of LSHR alloy with KWN model. The PanNickel database[40] was used for these simulations. This database provides the relevant thermodynamic model parameters and mobility data (modified based on the NIST mobility database[41]). The other input parameters for the kinetic models (e.g., the interfacial energy, molar volume and the nucleation site density) were optimized in terms of the available experimental data and stored in a separate XML precipitation database.

4.1 Early Stages of Precipitation in Ni-5.2Al-14.2Cr at.% Alloy

The addition of Cr to the binary Ni-Al system can significantly reduce the lattice parameter misfits between the precipitate phase (γ′) and the matrix phase (γ). In some Ni-Al-Cr alloys, the γ′ precipitates are nearly misfit free and remain spherical or spheroidal to fairly large sizes. A recent experimental study focusing on the earliest stages of decomposition in a model Ni-5.2Al-14.2Cr at.% alloy on a nanoscale using 3DAP microscopy and TEM was carried out by Sudbrack.[42] It was reported that the alloy decomposes into a high number density of nanometer-sized γ′ precipitates when aged at 600 °C. Figure 4(a) shows the predicated temporal evolution of γ′ number density compared with the measurements. It can be seen that the number density increases in the very early stages and reaches its maximum value of about 7×10^{24} at around 2 h, and subsequently decreases due to the coarsening effect. In the meantime, the evolution of the mean particle size as shown in Fig. 5(a) indicates that the mean radius initially remains almost same, and begins to grow after 1 h and then coarsen.

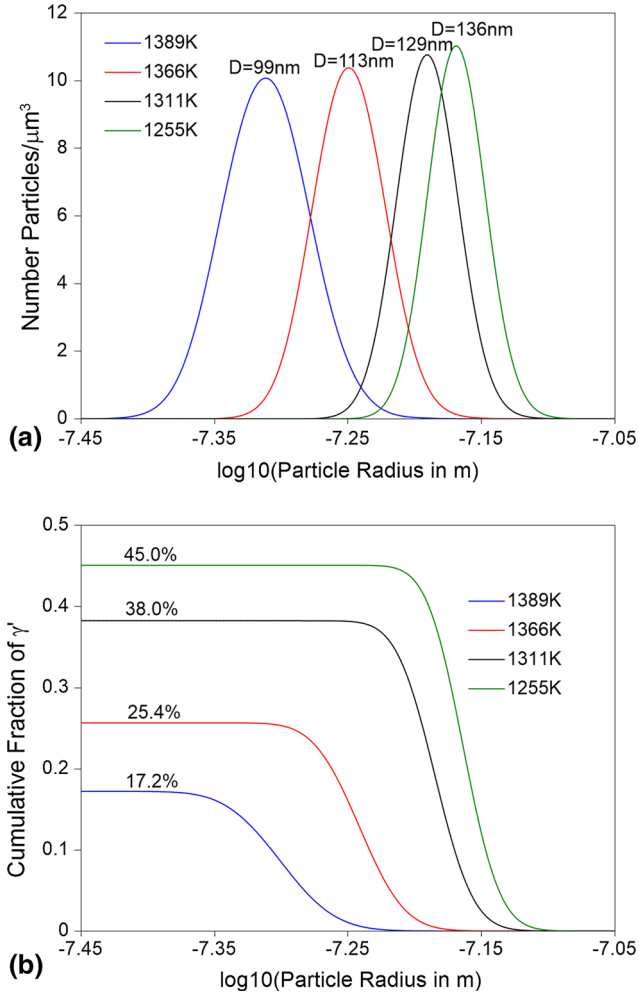

Fig. 11 Distribution and the cumulative fraction of γ' precipitates cooled to various temperatures at the speed of 139K/min

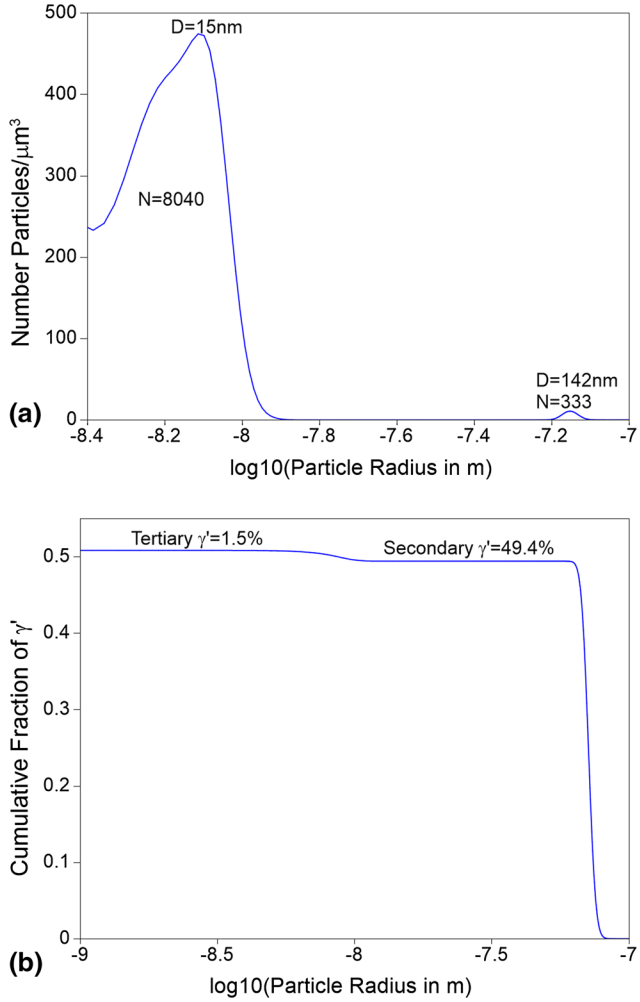

Fig. 12 Distribution and the cumulative fraction of γ' cooled to 1172K at the speed of 139K/min

Eventually, the coarsening effect becomes dominant after 16 h. After a long ageing time of 1024 h, the mean radius is around 7.7 nm and the equilibrium volume fraction 15.8% is nearly attained.

As has been pointed out for the case of the binary Ni-14 at.% Al alloy in section 3.1, nucleation, growth and coarsening occur concomitantly during the precipitation process. The correlation between the number density, particle size and volume fraction as shown in Fig. 4 and 5 suggest a strong concurrent process operating in the Ni-5.2Al-14.2Cr at.% alloy. A sharp increase in both number density and nucleation rate at a nearly constant mean particle radius is observed before 1 h, indicating that nucleation is the dominant mechanism over this time scale. Following the stage of rapid decreasing of the nucleation rate between 1 and 16 h, new nuclei are formed during this time period at a rate considerably smaller than the maximum value. In the meanwhile, stable nuclei grow and the mean particle size as well as the volume fraction increase accordingly. It should be noted that the peak number density is achieved after 2 h of ageing, and after that coarsening becomes significant while nucleation and growth are still going on. One can also verify that, the mean particle radius follows a linear relationship with $t^{1/3}$ after 16 h as shown in Fig. 5(c). This suggests that the coarsening effect plays the predominant role after 16 h and the nucleation rate is zero as shown in Fig. 4(b).

Figure 6 plots the predicated particle size distributions at 1.0, 8.4, and 10 and 25 h, which give an approximate understanding with regards to which mechanisms are dominating. For instance, in early stages of precipitation when nucleation dominates, the PSD is characterized by a sharp peak at around the critical radius, while at two intermediate times 8.4 and 10 h, the PSDs exhibit a bimodal shape due to a combined effect of the nucleation of new nuclei and the growth of established nuclei. It is noteworthy that such a bimodal shape has also been observed experimentally[42,43] and simulated by others.[19,22] As the transformation proceeds, the solute concentration in the matrix phase falls and the driving force for nucleation and growth decreases. As a result, the coarsening mechanism

takes over and the PSD will broaden and tend towards the steady state shape, which should be close to that predicated by the classical LSW theory. Two such PSDs are calculated and compared with the measurements as shown in Fig. 7, where the maximum particle frequency is normalized to be 1.0.

4.2 Coarsening of Rene88DT

Another example is shown for the simulation of coarsening behavior in a commercial alloy Rene88DT (Ni-1.99Al-12.99Co-15.67Cr-4.00Mo-3.88W-3.72Ti-0.70Nb in wt.%). Figure 8(a) shows the calculated phase fractions as a function of temperature together with the temperature window where the two phases γ^{+} γ' are stable and the experimental data are available. Figure 8(b) plots the cube of the predicated mean γ' size against time for five different temperatures 1080, 1050, 1020, 990 and 960 °C, obtained using the Fast-Acting model. In good agreement with the measured values by Mao,[44] the coarsening rate rises as the temperature increases. For each temperature, it is found that the γ' coarsening kinetics is consistent with the LSW theory even when the holding time is short, i.e., $t_0 \cong 0$ and R^3 is proportional to time.

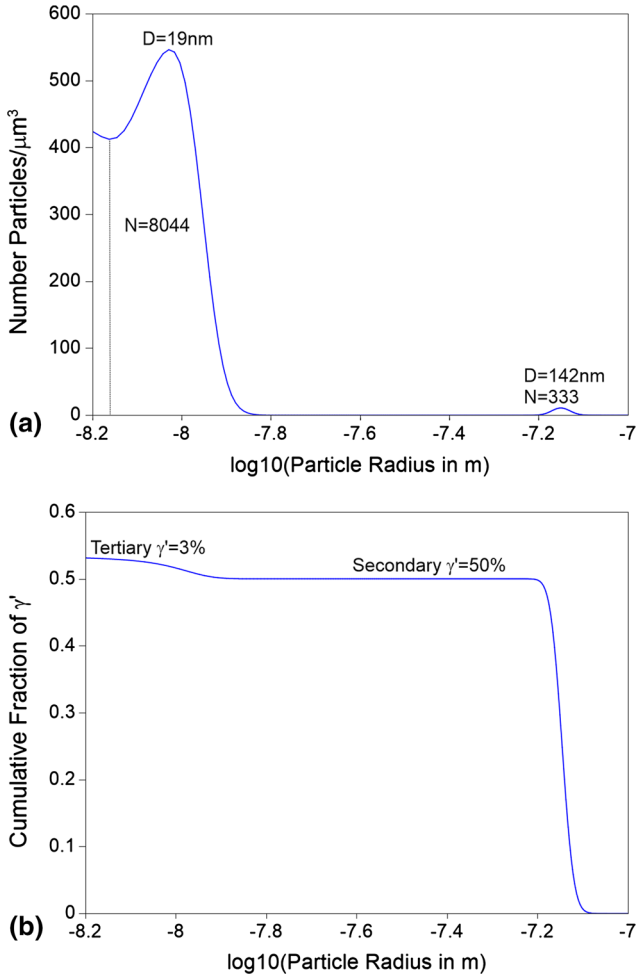

Fig. 13 Distribution and the cumulative fraction of γ' cooled to 1089 K at the speed of 139 K/min

4.3 Precipitation Kinetics of LSHR Alloy

Recently, Semiatin and colleagues[45] studied the high temperature precipitation behavior of a typical powder-metallurgy, γ/γ' nickel-base superalloy, LSHR. Table 1 lists the chemistry of the LSHR as used in their work. Figure 9 shows the calculated fractions of γ and γ' as a function of temperature using this chemistry. The fraction of γ' in this plot represents the total equilibrium fraction of γ' at each temperature, which may include primary, secondary and tertiary γ'. The calculated γ' solvus is 1422 K, which is in reasonable agreement with the measured γ' solvus: 1430 K. The calculated equilibrium fraction of γ' is ~2-3% higher than the measured ones, which may represent the small-sized tertiary γ' that was not counted in the experimental measurement. In Semiatin's study,[45] the LSHR samples

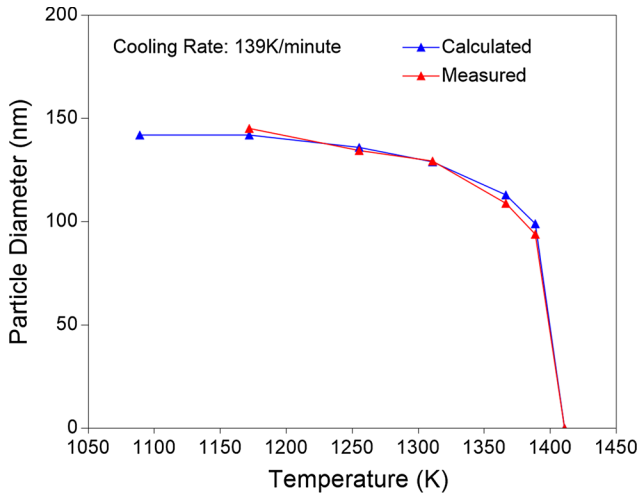

Fig. 14 Comparison of calculated and measured average γ' particle diameters

Table 2 Calculated and measured average γ' particle diameters at different temperatures

Temperature, K	1389	1366	1311	1255	1172	1089
Calculated, nm	99	113	129	136	142	142
Measured, nm	93.9	108.9	129.4	134.5	145.2	

Table 3 Calculated and measured number densities of secondary γ' particles when cooled to different temperatures (#/μm^3)

Temperature, K	1389	1366	1311	1255	1172	1089
Calculated, #/μm^3	339	333	334	339	333	333
Measured, #/μm^3	374	371.5	313.7	337.1	303.5	

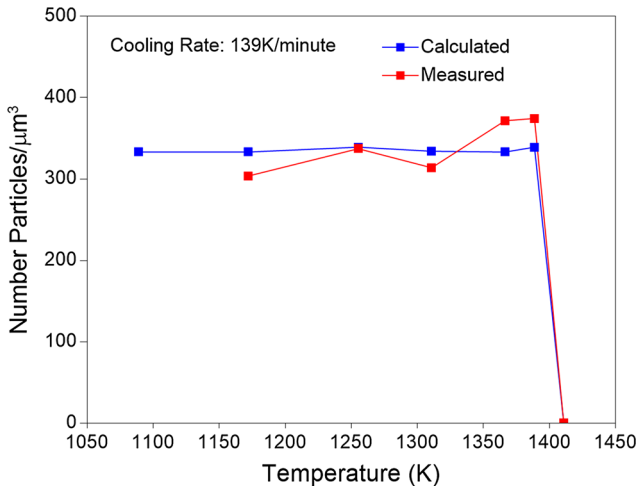

Fig. 15 Comparison of calculated and measured γ' number densities

were solutionized at supersolvus temperature: 1463 K for 20 min to dissolve γ' and homogenize the chemistry throughout the γ grain. These samples were then cooled at a rate (R_a) of 11 K/min or 139 K/min to a predetermined temperature (T_q) within the range of 1089 to 1411 K, then quenched.

Figure 10 shows the simulated results for the case of R_a =139 K/min and T_q = 1389 K. Figure 10(a) shows the particle size distribution, which indicates that the diameter of secondary γ' particles varies from 76 to 126 nm, and the diameter with highest population is 99 nm. Figure 10(b) shows the cumulative fraction of γ' precipitates as a function of particle size. It is seen that the total fraction of γ' is 17.2%. Similarly, simulations were performed for T_q = 1366, 1311, 1255 K with the same cooling rate R_a = 139 K/min. Figure 11 compares the particle size distributions and cumulative volume fractions of γ' precipitates when cooled to 1389, 1366, 1311, and 1255 K, respectively. As is seen, both the average size and the cumulative fraction of γ' increases as the temperature go lower. It should point out that no tertiary γ' precipitates were observed until 1255 K.

When cooled to 1172 K, the simulation showed the formation of tertiary γ' as shown in Fig. 12. It indicates that tertiary γ' started to precipitate between 1172 and 1255 K, which is consistent with experimental observation.[45] As shown in Fig. 12(a), the average diameter of secondary γ' is 142 nm, and the number density of secondary γ' is 333/μm^3; the average diameter of tertiary γ' is 15nm, and the number density of tertiary γ' is ~8040/μm^3. As shown in Fig. 12(b), the fraction of secondary γ' is 49.4% and the fraction of tertiary γ' is ~1.5%. When cooled to 1089 K, again the simulation showed the formation of tertiary γ'. As shown in Fig. 13(a), the average diameter of secondary γ' is 142 nm, and the number density of secondary γ' is 333/μm^3; the average diameter of tertiary γ' is 19 nm, and the number density of tertiary γ' is ~8044/μm^3. It should be pointed out that there are even smaller sized γ' particles which were not counted. As shown in Fig. 13(b), the fraction of secondary γ' is 50.0% and the fraction of tertiary γ' is ~3%.

Table 2 lists the measured and calculated γ' particle diameters (average) when cooled to different temperatures, and Fig. 14 compares the listed data in a plot. It is seen that the calculated average particle diameters agree with the measured ones very well. Table 3 lists the measured and calculated number densities of secondary γ' particles when cooled to different temperatures, and Fig. 15 compares the listed data in a plot. It is seen that the calculated number densities agree with the measured ones fairly well. Table 4 lists the measured and calculated fraction of secondary γ' precipitates when cooled to different temperatures, and Fig. 16 compares the listed data in a plot. It is seen that the calculated fraction of secondary γ' is 3-7% higher than the measured ones. On the other hand, since we assumed spherical γ' in the simulation, the calculated diameter, number density and fraction of secondary γ' satisfy the following equation:

$$f = \frac{4}{3}\pi\left(\frac{D}{2}\right)^3 \times N \qquad \text{(Eq 11)}$$

where D is the diameter and N the number density. Certainly the experimentally observed γ' are not regular sphere-shaped particles, it would be interesting to see what we will get if we calculate the fraction of secondary γ' using the measured diameter and number density of secondary γ' by Equation 11. In other words, we assume the experimental observed γ' particles are spherical. The fractions of γ' thus calculated are listed in Table 4. It is seen, the fractions of secondary γ' thus calculated are 2-6% higher than those directly measured and they agree with the model calculated values very well as shown by the green line (dots) in Fig. 16.

The effect of cooling rate on the precipitation behavior of LSHR was also studied in Semiatin's paper.[45] Calculations are performed in this study for a much slower cooling rate R_a = 11 K/min to 1389, 1366, 1311, and 1227 K. As is seen in Fig. 17, the following major differences were observed between the fast (139 K/min) and the slow (11 K/min) cooling rates: (i) slow cooling rate leads to bimodal distribution of secondary γ', (ii) slow cooling rate leads to much bigger particle size of secondary γ' (~3 times as big

Table 4 Calculated and measured fraction of secondary γ' particles when cooled to different temperatures (mole/-mole)

Temperature, K	1389, %	1366, %	1311, %	1255, %	1172, %	1089
Calculated	17.2	25.4	38.0	45.0	49.5	50.0
Measured	14.1	21.8	30.9	37.3	42.2	
Calculated by Equation 13	16.2	25.1	35.6	42.9	48.6	

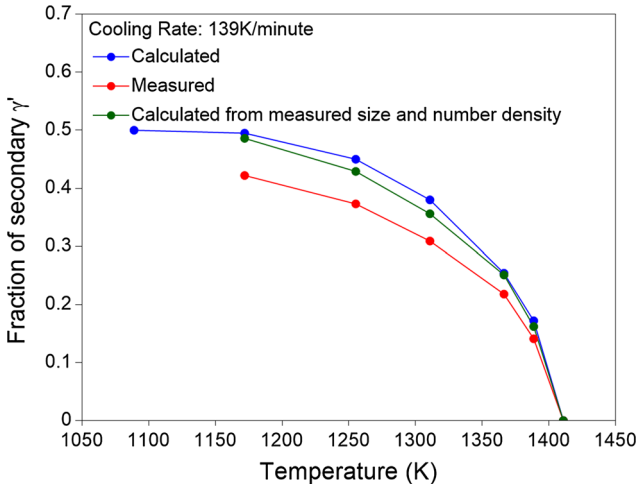

Fig. 16 Comparison of calculated and measured fraction of secondary γ'

as the fast cooling rate), (iii) slow cooling rate leads to slightly higher volume fraction of secondary γ'.

5. Concluding Remarks

An integrated computational thermodynamics and kinetics approach was explored in this study to simulate the microstructural evolution of nickel-based alloys during the precipitation process. The unique feature of this work is that the multi-component phase equilibrium and mobility information required by microstructural modeling are directly obtained from thermodynamic calculation engine based on the CALPHAD method. Therefore, no prior assumption needs to be made with regard to the thermodynamics of multi-component alloys. The simulated microstructure features, such as volume fraction, average particle size and particle size distribution, can further be coupled with the age hardening model to simulate the corresponding mechanical properties. This leads to great confidence for the applications of this modeling approach to multi-component commercial alloys for industrial solutions. The functionalities and advantages of this approach have been demonstrated by the precipitation simulation of multi-component nickel-based alloys.

Nevertheless, it is never too much to emphasize the importance of the related thermodynamic/mobility and precipitation databases in order to make reliable simulations. The precipitation kinetics is sensitive to the input parameters

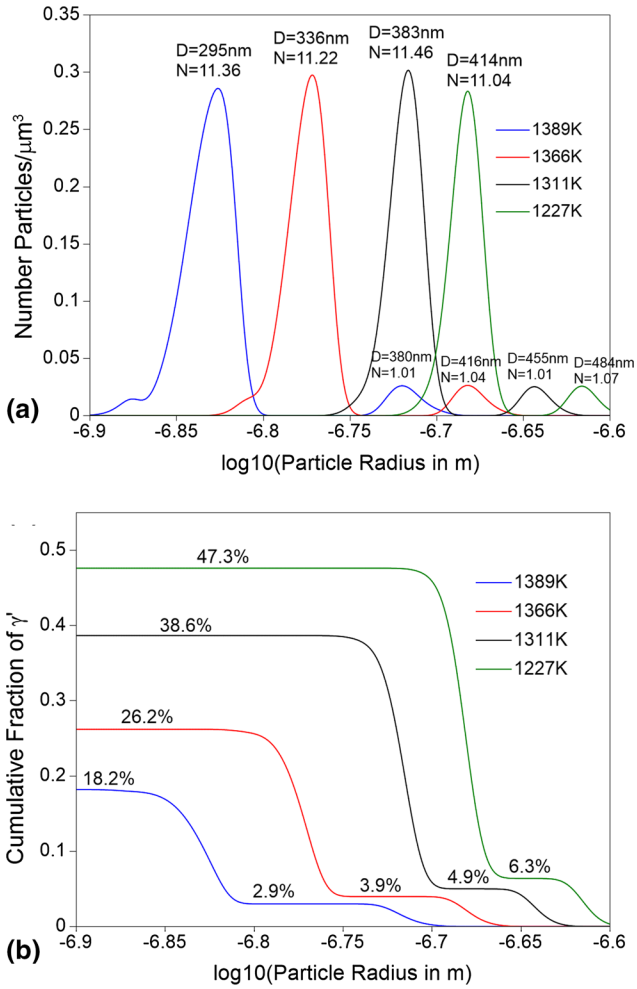

Fig. 17 Distribution and the cumulative fraction of γ' precipitates cooled to various temperatures at the speed of 11 K/min

particularly to the value of the interfacial energy, which is usually difficult to be measured directly by experiments. One must perform extensive validations so that the chosen parameters could reasonably describe the precipitation behavior of the key alloys with abundant experimental data. The precipitation databases containing all these parameters are still under development. Even though the CALPHAD calculation, combined with the thermodynamic/mobility database, shows rather good predictive capability in obtaining the necessary thermodynamic properties and diffusivity data, it could still be risky when the calculation is outside the assessed composition ranges.

ACKNOWLEDGMENTS

The authors acknowledge the financial support of US Air Force through the SBIR Phase I and Phase II contracts: FA8650-04-M-5208 and FA8650-05-C-5202. We would especially like to thank Dr. Jeff Simmons and his colleagues of the AFRL at Wright-Patterson for their continuing interest in this work.

Reference

1. L. Kaufman and H. Bernstein, *Computer Calculation of the Phase Diagrams with Special Reference to refractory Materials*, Academic Press, New York, 1970
2. J. Allison, D. Backman, and L. Christodoulou, *JOM*, 2006, **58**(11), p 25-27
3. Z.-K. Liu, L.-Q. Chen, and K. Rajan, *JOM*, 2006, **58**(11), p 46-50
4. K. Rajan, *Mater. Today*, 2005, **8**(10), p 38-45
5. A.J. Ardell, *Metall. Mater. Trans. A*, 1985, **A16**, p 2131
6. A. Deschamps and Y. Brechet, *Acta Mater.*, 1998, **47**(1), p 293-305
7. S. Esmaeili, D.J. Lloyd, and W.J. Poole, *Acta Mater.*, 2003, **51**(8), p 2243-2257
8. J. Friedel, *Dislocations*, Pergamon, Oxford, 1964
9. R. Kampmann and R. Wagner, Kinetics of Precipitation in Metastable Binary Alloys - Theory and Application to Cu-1.9at%Ti and Ni-14at%Al, *Decomposition of Alloys: The Early Stages*, P. Haasen et al., Ed., Pergamon Press, Oxford, 1984, p 91-103
10. I.M. Lifshitz and V.V. Slyozov, *J. Phys. Chem. Solids*, 1961, **19**, p 35
11. O.R. Myhr, Ø. Grong, and S.J. Andersen, *Acta Mater.*, 2001, **49**(1), p 65-75
12. J.D. Robson, *Acta Mater.*, 2004, **52**, p 4669-4676
13. J.D. Robson, M.J. Jones, and P.B. Prangnell, *Acta Mater.*, 2003, **51**(5), p 1453-1468
14. J.S. Langer and A.J. Schwartz, *Phys. Rev. A*, 1980, **21**(3), p 948-958
15. M. Avrami, *J. Chem. Phys.*, 1939, **7**(12), p 1103-1112
16. M. Avrami, *J. Chem. Phys.*, 1940, **8**(2), p 212-224
17. M. Avrami, *J. Chem. Phys.*, 1941, **9**(2), p 177-184
18. A.N. Kolmogorov, *Izv. Acad. Sci. SSSR Ser. Math.*, 1937, **3**, p 355-360
19. J.D. Robson, *Mater. Sci. Technol.*, 2004, **20**, p 441-448
20. M. Starink, *J. Mater. Sci.*, 1997, **32**(15), p 4061-4070
21. C. Wagner, *Acta Metall.*, 1954, **2**(2), p 242-249
22. W. Cao, S.L. Chen, F. Zhang, K. Wu, Y. Yang, Y.A. Chang, R. Schmid-Fetzer, and W.A. Oates, *Calphad*, 2009, **33**(2), p 328-342
23. Wu, K.S., Zhang, F., Chen, S.L., Cao, W.S., and Chang, Y.A. *A modeling tool for the precipitation simulations of superalloys during heat treatments*. in *11th International Symposium on Superalloys*. 2008. Champion, PA
24. S.L. Chen, S. Daniel, F. Zhang, Y.A. Chang, X.Y. Yan, F.Y. Xie, R. Schmid-Fetzer, and W.A. Oates, *Calphad Comput. Coupling Phase Diagr. Thermochem.*, 2002, **26**(2), p 175-188
25. W.A. Johnson and R.F. Mehl, *Trans. Am. Inst. Min. Metall. Eng.*, 1939, **135**, p 416-458
26. Gerold, V (1979) Precipitation hardening. In *Dislocations in solids*. North Holland: Amsterdam
27. Y.A. Chang, S.L. Chen, F. Zhang, X.Y. Yan, F.Y. Xie, R. Schmid-Fetzer, and W.A. Oates, *Prog. Mater. Sci.*, 2004, **49**(3-4), p 313-345
28. I. Ansara, *Int. Met. Rev.*, 1979, **24**, p 20-53
29. I. Ansara, B. Sundman, and P. Willemin, *Acta Metall.*, 1988, **36**(4), p 977-982
30. M. Hillert, B. Jansson, B. Sundman, and J. Ågren, Metall, *Trans. A*, 1985, **16A**(2), p 261-266
31. W. Cao, Y.A. Chang, J. Zhu, S. Chen, and W.A. Oates, *Acta Mater.*, 2005, **53**(2), p 331-335
32. W.A. Oates, F. Zhang, S.L. Chen, and Y.A. Chang, *Phys. Rev. B*, 1999, **59**(17), p 11221-11225
33. F. Zhang, Y.A. Chang, Y. Du, S.L. Chen, and W.A. Oates, *Acta Mater.*, 2003, **51**(1), p 207-216
34. R. Kikuchi, *Phys. Rev.*, 1951, **81**, p 988
35. C.E. Campbell, W.J. Boettinger, and U.R. Kattner, *Acta Mater.*, 2002, **50**, p 775-792
36. O. Redlich and A.T. Kister, *Ind. Eng. Chem.*, 1948, **40**, p 345-348
37. E. Kozeschnik, I. Holzer, and B. Sonderegger, *J. Phase Equilibria Diffus.*, 2007, **28**(1), p 64-71
38. J.E. Morral and G.R. Purdy, *Scr. Metall. Mater.*, 1994, **30**(7), p 905-908
39. C. Wagner, *Z. Elektrochem.*, 1961, **65**, p 581
40. PanNickel, Thermodynamic database for multicomponent nickel alloys, CompuTherm LLC, Middleton, WI, 2009. www.computherm.com
41. *NIST Diffusion Data Center*. http://patapsco.nist.gov/diffusion/
42. Sudbrack, C.K. (2004) Decomposition behavior in model Ni-Al-Cr-X superalloys: Temporal evolution and compositional pathways on a nanoscale. In Materials Science and Engineering. Northwestern University: Evanston, IL. p. 235
43. S.Q. Xiao and P. Haasen, *Acta Metall. Mater.*, 1991, **39**(4), p 651-659
44. Mao, J (2002) *Gamma Prime Precipitation Modeling and Strength Responses in Powder Metallurgy Superalloys*, Ph. D. Thesis, College of Engineering and Mineral Resources at West Virginia University, p. 94
45. S.L. Semiatin, S.-L. Kim, F. Zhang, and J.S. Tiley, *Metall. Mater. Trans.*, 2015, **46A**, p 1715-1730